Correction for meteor centroids observed using rolling shutter cameras

Patrik Kukić[1], Peter Gural[2], Denis Vida[3,4], Damir Šegon[5], and Aleksandar Merlak[6]

As the currently prevalent analog CCD sensors used in meteor cameras are being phased out by manufacturers, amateur meteor astronomers have been investigating the use of low-cost CMOS alternatives. Many CMOS cameras in the lower price range (<100 USD) have a top-to-bottom, sequentially delayed exposure start time (rolling shutter) which can influence meteor centroids and subsequently the estimation of meteor dynamics. Here we present two methods, one temporal and one spatial, of correcting for the rolling shutter effect and demonstrate the correction in practice. The code used to demonstrate the effects and corrections is available on GitHub (`https://github.com/PKukic/RollingShutterSim`). We show that the rolling shutter effect, although minor for moderate field of view meteor video systems, can be corrected for and that the correction residuals are within the image centroid measurement accuracy.

Received 2018 July 25

1 Introduction

Currently prevalent CCD sensors, that are used in video meteor cameras, are starting to be phased out. In 2015 Sony announced they would discontinue manufacturing all CCD sensors by 2020 and completely focus on CMOS technology. Since most meteor networks use analog video cameras with Sony CCD sensors (Brown et al., 2010; Jenniskens et al., 2011; Samuels et al., 2014), the announcement has a significant impact on the meteor community.

In the domain of progressive scan CMOS sensors, all circa 2018 low-cost sensors (<100 USD) have rolling shutters, while only the more expensive cameras use a global shutter technology (e.g. the Sony Pregius line of CMOS cameras). A CMOS global shutter behaves like a CCD sensor, in that each pixel starts and stops its exposure at the same time. In rolling shutter cameras, each sensor row of pixels starts their exposure a fixed delay after the previous row's pixels (temporal delay of $1/(n_{rows} \times FPS)$, e.g. in the case of a 720p camera operated at 25 FPS the time delay is 56 µs), thus each pixel row represents a different time window. The exposure for each row stops a fixed integration time after the start, which can vary from a few microseconds to as high as the frame-to-frame time (1/FPS) of the sensor. The rolling shutter exposure delays per row distorts fast-moving objects, since each pixel row has captured the moving object at a different time and spatial position. In global shutter cameras, since all pixels start and stop their integration simultaneously, they are effectively taking a snapshot of the object at a single instant in time. Most of the previously used analog CCD cameras had interlaced video which influenced meteor centroids in a different way due to alternating missing rows. But they in fact offered double the temporal resolution by sacrificing half the vertical resolution (e.g. 50 half frames (fields) per second instead of 25 frames per second) (Vida et al., 2016). Progressive scan CMOS sensors do not use interlacing thus avoiding missing rows in the centroid estimate. Figure 1 illustrates the difference between various exposure methods of global shutter, interlaced, and rolling shutter. It should be noted that the reason for the rolling shutter design resides in the simple and efficient approach to sequentially read each row in a time delayed fashion.

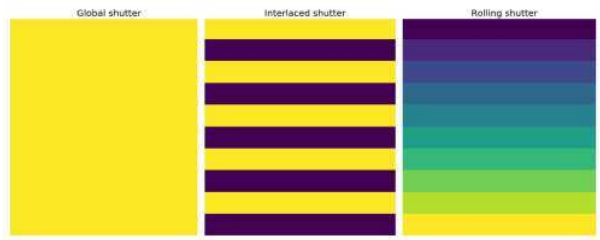

Figure 1 – Left: Global shutters read out the whole image at once at $1/FPS$ intervals. Middle: The reading of alternating odd and even rows in interlaced video occurs in $1/(2 \times FPS)$ intervals. Right: Every row in the rolling shutter is exposed and read out sequentially, $1/(n_{rows} \times FPS)$ seconds after the other.

The centroid of a meteor streak captured by a rolling shutter camera will shift relative to the global shutter centroid along the meteor's direction of motion, which is dependent on angle and apparent angular velocity on the focal plane. Horizontal meteors have no centroid shift because the "reader" (the leading edge of pixel integration) meets the meteor in regular time intervals of $1/FPS$, while centroids of vertical meteors are affected the most because the reader meets them at constantly changing time intervals. Note that this effect is similar to the effect of a mechanical rotating shutter used by photographic fireball networks in the past, which also had to be corrected for (Ceplecha, 1987).

It should be noted that rolling shutter is even more distorting if the camera is slewing or jittering as in a hand held cell phone video. It will appear to look like viewing through "jello" and involves more sophisticated corrections than we present here for a fixed mounted meteor camera. For meteors, the rolling shutter impacts the vertical spread of the meteor, stretching the meteor

[1]XV Gymnasium, Jordanovac 8, HR-10000 Zagreb, Croatia
[2]Gural Software Development
[3]Department of Earth Sciences, University of Western Ontario, London, Ontario, N6A 5B7, Canada
[4]Department of Physics and Astronomy, University of Western Ontario, London, Ontario, N6A 3K7, Canada
[5]Astronomical Society Istra Pula, Park Monte Zaro 2, HR-52100 Pula, Croatia
[6]ISTRA STREAM d.o.o., Hum, Croatia

IMO bibcode WGN-465-kukic-rolling
NASA-ADS bibcode 2018JIMO...46..154K

streak when it moves downward, fore-shortening when it moves upwards, with a bias in the direction of motion.

In this paper we investigate rolling shutter effects on meteor centroids by creating synthetic meteor videos and simulating the rolling shutter effect. We develop two methods of centroid correction (temporal and spatial) and demonstrate that both produce corrected centroids which are within the centroid measurement uncertainty. The corrections can account for the integration time being less than the frame-to-frame time.

2 Methods

2.1 Simulating meteors and rolling shutter effects

In this section we discuss details of the meteor simulation. Two independent simulations were developed to validate results, but only one will be described herein. The meteor was represented as a propagating streak along a line that passed through the centre of the image. The duration of the meteor was estimated using the apparent angular velocity of the meteor ω (in units of '/s) and a pixel scale k (in units of '/px). A square-pixel, non-warped image scale was calculated by dividing one dimension of the field of view (FOV) in degrees with one dimension of the image resolution:

$$k = (60'/^\circ)\frac{\theta_h}{X_{size}} \approx (60'/^\circ)\frac{\theta_v}{n_{rows}} \tag{1}$$

where θ_h and θ_v are horizontal and vertical sizes of the FOV in degrees, while X_{size} and n_{rows} are the horizontal and the vertical image resolution, respectively. We modeled a camera with the resolution of 1280×720, a FOV of $42^\circ \times 24^\circ$, which corresponds to a 6 mm $f/1.2$ lens. This gave a pixel scale of $k \approx 2$ '/px. To simulate the effect of meteor deceleration, the meteor's angular velocity at a given point in time was computed using the empirical exponential deceleration model by Jacchia & Whipple (1961):

$$\omega(t) = \omega_0 - ab\exp(bt) \tag{2}$$

where ω_0 is the initial angular velocity of the meteor, measured in '/s, and a ['] and b[s^{-1}] are the deceleration coefficients. In the case of a constant velocity meteor, a or b are 0. Given the difference between the initial angular velocity ω_0 and a final angular velocity $\omega(t)$, deceleration parameters can be computed. Rearranging the equation (2) gives the following expression:

$$\Delta\omega = \omega_0 - \omega(t) = ab\exp(bt) \tag{3}$$

If we keep a fixed, b can be found using the following equation:

$$b = \frac{\Re\left(W\left(\frac{t}{a}\left(\omega_0 - \omega(t)\right)\right)\right)}{t} \tag{4}$$

where $\Re$ denotes the real part of the Lambert-W function. Several deceleration profiles based on various velocity differences ($\Delta\omega$) are shown in Figure 2 (the a parameter was fixed at $0.06'$, and the b parameter was computed). In all our simulations we have assumed that the meteor will decelerate 10% from its initial velocity.

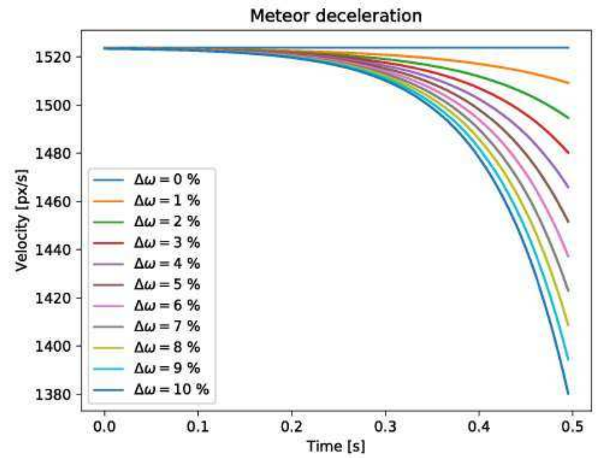

Figure 2 – Several exponential deceleration profiles based on different velocity losses. The velocity loss is expressed as a percentage of the initial meteor velocity.

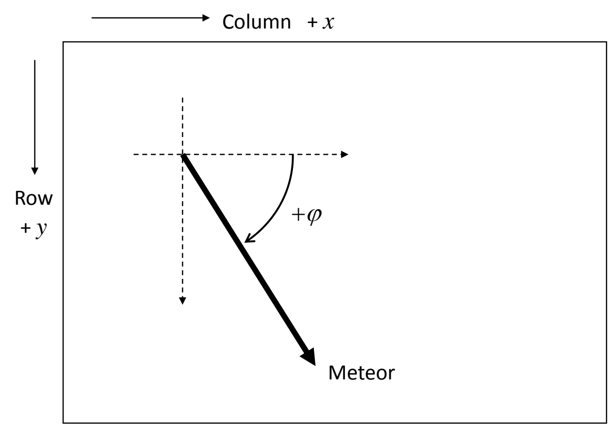

Figure 3 – The image coordinate system.

Next, the distance from the image centre at time t, $R(t)$ is calculated as:

$$R(t) = \frac{\omega(t)t}{k} \tag{5}$$

The coordinates of the points on the line are transformed from polar to Cartesian image coordinates (x, y) using the following equations:

$$\begin{aligned} x &= x_{center} + R\cos\varphi \\ y &= y_{center} + R\sin\varphi \end{aligned} \tag{6}$$

where x_{center} and y_{center} are the coordinates of the image centre and φ is the angle of the meteor from the horizontal, measured positive clockwise. Note that the origin of this system is in the upper left-hand corner of the image, and that the Y axis has been inverted. Figure 3 illustrates the coordinate system.

The total number of frames is computed as a ratio of the duration of the meteor and frames per second (FPS). In our simulation we used the FPS of 25. The

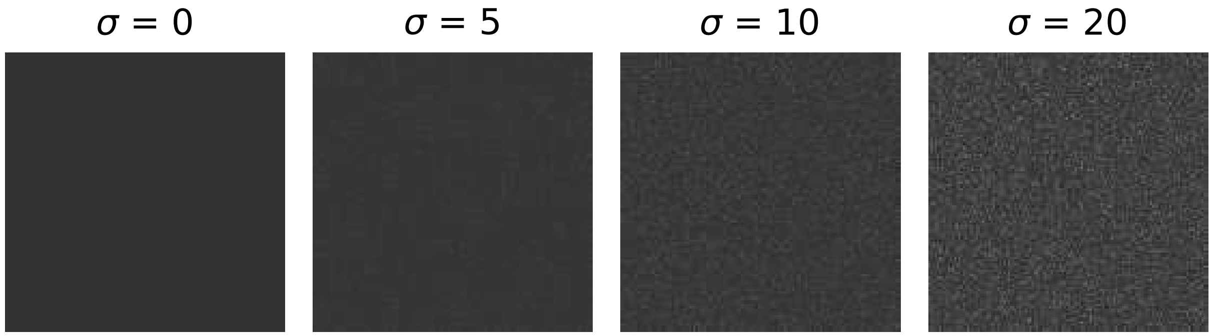

Figure 4 – From left to right: Background noise levels of 0, 5, 10 and 20.

duration is computed from the angle and meteor's angular speed, making sure the computed positions are always within the image. We considered every computed position of the meteor as a light source approximated by a Gaussian point spread function (PSF) which was evaluated and added to the simulated video frame matrix. The following formulation of a two-dimensional Gaussian function was used:

$$f(x, y) = A \exp\left(-\left(\frac{(x - x_0)^2}{2\sigma_x^2} + \frac{(y - y_0)^2}{2\sigma_y^2}\right)\right) \quad (7)$$

where A is the amplitude which we keep at unity, (x_0, y_0) are the coordinates of the centre of the Gaussian, and σ_x and σ_y are standard deviations along the respective axes. To speed up the computation, we only evaluate the Gaussian within a 3σ window from its centre, as any values outside that window are effectively 0. We used the values of standard deviations of $\sigma_x = \sigma_y = 2$ px. To simulate the meteor trail, we compute the position of the meteor on hundreds of fine spatial steps between the beginning and the end of the frame, evaluate the PSF to every point and integrate them.

After the simulated frame integration was done, Gaussian noise was added to the image to simulate the readout noise. The intensity integration was performed using a floating point matrix. We scaled the peak intensity of the image to 255 and converted the image to an 8-bit unsigned integer to simulate the digitization process. This way we made sure all simulated meteors are of the same brightness regardless of speed and also prevented saturation effects.

Finally, the simulated frame was generated by reading out the sensor image matrix via either a global or a rolling shutter. When reading out the image with a global shutter, the whole sensor image was read out at once, hence the read out frame was equal to the sensor image matrix. When reading out the sensor image matrix with a rolling shutter, the following method was used: the first frame of the meteor was used as an initialization frame, thus ensuring all rows have equal exposure time. The readout started with the second frame, where the image rows were read out top to bottom with a temporal shift of $1/(720 \times 25) = 55$ µs after the sensor image matrix was updated for that temporal shift. Immediately after a specific row was read out, the values in that same row of the sensor image matrix were reset to 0.

The coordinates of the meteor on each simulated frame were computed by centroiding the meteor streak. The centroid in the X dimension was computed as:

$$x_{centroid} = \frac{\sum_{x=0}^{N} \sum_{y=0}^{M} x \left(I_{x,y} - I_{noise}\right)}{\sum_{x=0}^{N} \sum_{y=0}^{M} \left(I_{x,y} - I_{noise}\right)} \quad (8)$$

where (N, M) is the size of the centroiding window (we only centroided everything inside 3σ from the extreme points on the meteor track), $I_{x,y}$ is the pixel intensity at position x, y) and I_{noise} is the background noise intensity. The background noise intensity is estimated as the mean value of all pixel intensities outside the meteor window. This same approach was used to find the centroid in the Y dimension with the numerator term x replaced by y.

After developing the simulation, it was tested by generating multiple meteors with their velocities ranging from 5 to 50°/s (a range of meteor angular velocities one might observe on the sky), while their angle was fixed at a value of 45°. For a scale of 2 '/px, the on-chip meteor velocities were thus in the range of 150 to 1500 px/s. The influence of four different levels of background noise on centroid estimation was performed by adding Gaussian noise with standard deviations of: 0 (no noise), 5, 10, and 20 to the imagery. Figure 4 shows a sample of every simulated background noise level.

We computed the centroids from the images with different background noise levels and compared them to the known modeled centroid values. The results are shown in Figure 5. The centroid offset (that is, the distance between the real and computed centroid point) was under 0.2 pixels even with the highest modeled noise level. Please note that these are the best case centroid values as we used the highest signal-to-noise ratio of an sensor with 8 bit dynamic range (all meteor peaks were at the level of 255), the real-world values may be worse. We show similar graphs later in the paper for corrected centroids to demonstrate the feasibility of the proposed correction methods in the presence of noise.
Next was an investigation on the influence of a simulated rolling shutter on meteor centroids, by simulating several meteors with various angles and angular veloci-

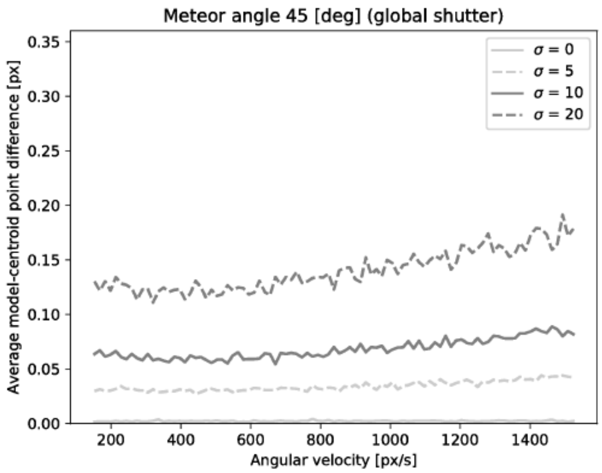

Figure 5 – Theoretical ideal centroid precision, depending on meteor velocity and noise level.

ties. We noted that when captured by a rolling shutter, the meteor centroids moved relative to the true centroid along the direction of the motion of the meteor. One example is shown in Figure 6. The simulated meteor was moving from upper left to lower right. In the top half of the image, the centroids are behind the true (model) position in the direction of motion, (they are behind the center of the global shutter gray streak), at approximately half the image height in pixels the centroid is located close to the center of the global track, and at the bottom half the rolling shutter centroid is now leading the true mean position of the meteor. The consequences of this behavior is that the velocity estimate from a rolling shutter will be larger than for the same meteor seen from a global shutter! If the meteor were moving upwards, the velocity would appear to be smaller for rolling versus global.

Next, we repeated the analysis of centroids and noise levels, but this time with the rolling shutter effect included. In contrast to the results obtained in the global shutter simulations, the maximum centroid offset was just under 30 pixels and its value was proportional to the meteor's on-chip velocity, as shown in Figure 7. Note that all noise levels on the figure are all on top of one another as the rolling shutter effect dominates the centroid difference for the plot scale used.

These results show that the rolling shutter significantly influences positions of centroids along the direction of the meteor's motion for meteors with a high apparent velocity, and that a correction is needed to have accurate centroid coordinates and thus correct velocity estimation. The relationship between the meteor's angle, the centroid's Y coordinate and the centroid offset was also investigated. A meteor was simulated for each angle from 0° to 360°, while its velocity was fixed at a high value of 1500 px/s, the results are shown in Figure 8. We noticed that the meteor angle does not influence the direction of the centroid offset – they are distributed along the line on the plot. Instead, the amount of centroid offset was found to be inversely proportional to the Y coordinate of the meteor centroid.

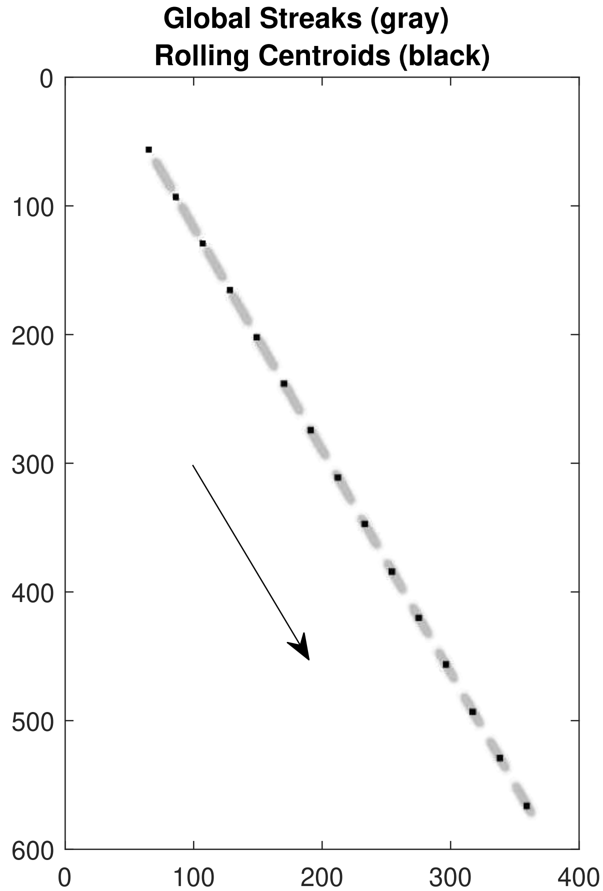

Figure 6 – Rolling shutter centroids changing position relative to the center of global shutter tracks.

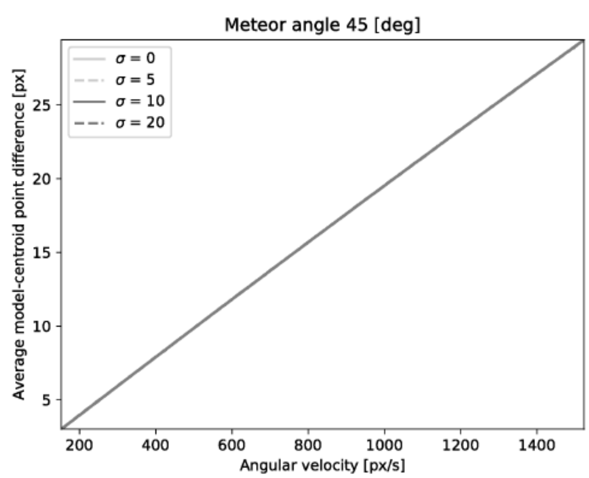

Figure 7 – Centroid offset in relation to the meteor velocity (given in px/s). The centroid offset dominates, thus all noise levels share the same line.

Based on these results, two methods of meteor centroid correction were developed. A temporal correction which corrects the time of a given centroid using minimal information (Section 2.2), and a spatial correction which corrects the image coordinates of the centroid with a uniform time sampling, but requires estimating the meteor angle and instantaneous velocity from the imagery (Section 2.3).

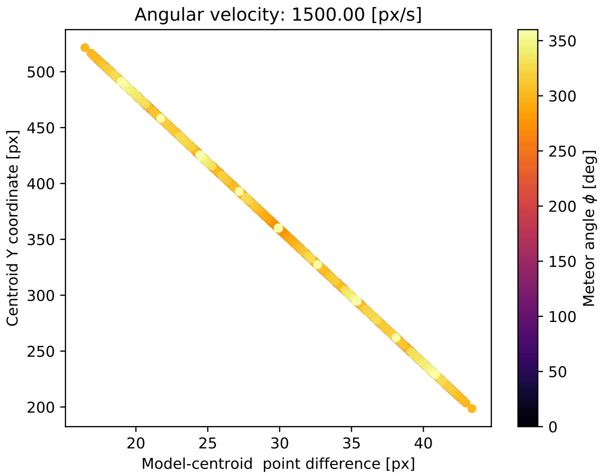

Figure 8 – The velocity is fixed at an extreme value of 1500 px/s, while the Y coordinate of the centroid and the correction distance are plotted. Different meteor angles are shown in different colors, but not all colors are visible because they overlap each other.

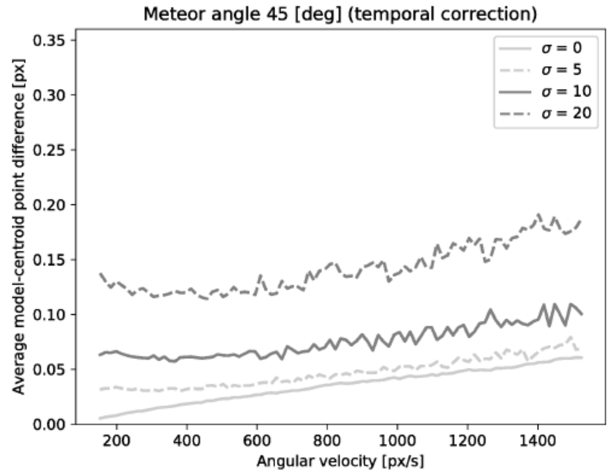

Figure 9 – The centroid offset in relation to the velocity. The temporal correction is applied to the centroid coordinates.

2.2 Temporal correction

Because the centroid offset is highly dependent on the vertical position of the meteor on the image, it is possible to correct for the rolling shutter effect by simply modifying the time stamps of the centroids. This of course will result in a variable time sampling out of sync with the frame time for each centroid position of each meteor image, rather than the uniform time sampling experienced with a global shutter.

First, it should be noted as to the way absolute time is computed from video frames. For global shutters this should be the middle of the exposure period for a given frame. For rolling shutters care must be taken to account for exposure times less than the frame time and when a camera time stamps the image. For now, we will assume that any small bias in absolute time will be corrected for later during trajectory estimation. Thus the relative time of every frame from some reference time can be computed with the following equation:

$$t_{frame} = \frac{i_{frame}}{FPS} \tag{9}$$

where i_{frame} is the index of the frame since the beginning of the meteor, and FPS is the frames per second of the camera.

In rolling shutter cameras, each pixel row starts its exposure at a slightly later time after the row above, and the time delay between each pixel row depends on the number of rows in the image. The time delay between the start of each subsequent row is:

$$\Delta t = \frac{1}{FPS}\frac{1}{n_{rows}} \tag{10}$$

where n_{rows} is the size of the image's Y axis in pixels (i.e. the vertical dimension). Assuming that the rolling shutter starts integrating from the top, the time of every row y_i is then:

$$t_{row} = y_i \Delta t \tag{11}$$

The Y coordinate of the meteor centroid hence determines the time at which the meteor centroid was captured. Including a time bias t_f based on f, the ratio of exposure time to the frame-to-frame time divided by the frame rate FPS, corrects the rolling shutter time into one that is synchronized with a global shutter (assumes the rolling shutter centroids are computed just after the last row is read out). f was defined as:

$$f = t_{exposure} FPS \tag{12}$$

where $t_{exposure}$ is the exposure time.

The rolling shutter centroids will thus fall on the global shutter track at the appropriate time. It only remains for the user to determine the global shutter bias relationship to absolute time. Thus the corrected relative time can be computed as:

$$t'_{frame} = t_{frame} - t_{row} - t_f = \frac{1}{FPS}\left(i_{frame} - \frac{y_i}{n_{rows}} - f\right) \tag{13}$$

where y_i is the Y coordinate of the rolling shutter centroid.

The performance of the temporal correction was tested by applying it to simulated centroids of noisy, decelerating meteors with an angle of $\varphi = 45°$ and a range of velocities. The final meteor velocity was 90% of the initial velocity, and the duration of the meteor was a multiple of the frame time ($1/FPS$). The a parameter used to model meteor deceleration was fixed at the value of 0.06', while the b parameter was computed using methods described in Section 2.1. We computed the difference in pixels from the true (model) and computed centroid positions. The results are shown in Figure 9. The maximum centroid offset for the highest velocity and the highest level of background noise is under 0.2 pixels, which is comparable to the achievable precision. Only for the highest angular velocities does the correction start to slightly deviate from the theoretical precision.

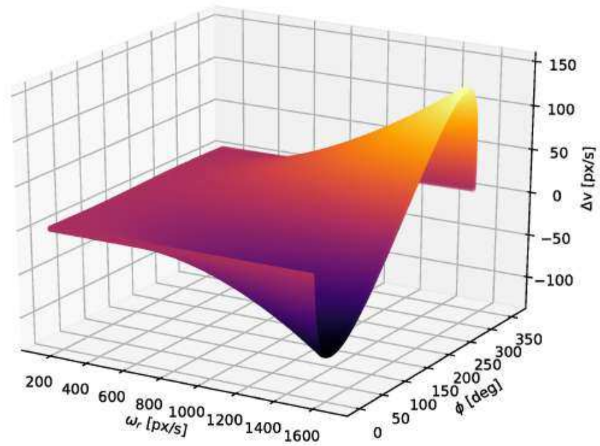

Figure 10 – The dependence of the angular velocity shift on the meteor angle and the observed angular velocity.

2.3 Spatial correction

For certain applications one might want to correct the location of the centroid instead of its time, for example if it is absolutely essential that the points are equally spaced in time as assigned by a frame time. The spatial correction is more complex and involves estimating two parameters of a meteor: the instantaneous angular velocity at every centroid (ω_i) and the meteor angle (φ).

The meteor angle φ was found by fitting a line in the parametric form relating Cartesian to polar coordinates (equation (6), R and φ are fitted) to Y coordinates of centroids versus the distance from the beginning of the meteor – the first centroid at (x_0, y_0) has a distance 0, the final centroid has a distance equivalent to the length of the meteor track.

Next, the instantaneous velocity (ω_i) for each centroid is calculated using the following equation:

$$\omega_i = \frac{\Delta r}{\Delta t} = \frac{r_i - r_{i-1}}{t_i - t_{i-1}} \tag{14}$$

Note that this velocity is given in px/s, rather than '/s. This set of velocities was then smoothed out as instantaneous velocities are sensitive to small measurement errors in centroids. A new value was assigned to each velocity, which was equal to the mean of its two neighbouring velocities:

$$\bar{\omega}_i = \frac{\omega_i + \omega_{i+1}}{2} \tag{15}$$

As the first point does not have a predecessor, we assumed that $\bar{\omega_0} = \bar{\omega_1}$.

Meteors were simulated with velocities ranging from 150 to 1500 px/s, and meteor angles from 0° to 360° using the rolling shutter simulation. We compared the observed angular velocities (computed centroid of the simulated rolling shutter frames) and known angular velocities obtained from equation (2) and found they did not match. In fact, as the rolling shutter effect shifts both the position and the time assigned to each centroid, the angular velocities are also shifted. Computing the difference between the known velocity and the rolling shutter impacted velocity (i.e. the velocity shift), it was found that it is a function of the meteor angle and the observed velocity. The plot of the function is shown in Figure 10. The velocity difference is 0 for a meteor travelling horizontally ($\varphi = 0°$ or $\varphi = 180°$) as the reader meets the meteor in regular intervals. But if the meteor's motion has a vertical component, the reader meets it at different time intervals and the apparent angular velocity changes.

The following equation models this velocity shift, i.e. the value by which the centroid velocity has to be corrected to obtain the true velocity:

$$\Delta\bar{\omega}_i(\bar{\omega}_i, \varphi) = -\bar{\omega}_i \frac{p}{p+1} \tag{16}$$

where p is defined as:

$$p = \sin\varphi \frac{\bar{\omega}_i}{\omega_{ref}} \tag{17}$$

The value of ω_{ref} is defined either as n_{rows} (if the velocity is measured in pixels/frame), as $n_{rows} \times FPS$ (if the velocity is measured in pixels/second) or as $n_{rows} \times FPS \times k$ (if the velocity is measured in arcminutes per second). Here, n_{rows} is the vertical dimension of the image, and FPS is the number of frames per second taken by the camera. Hence the corrected velocity value is:

$$\omega_{corr(i)} = \bar{\omega}_i + \Delta\bar{\omega}_i \tag{18}$$

As it can be seen from Figures 7 and 8, the correction distance is proportional to the meteor's velocity and inversely proportional to its Y coordinate. Additionally, the distance correction was found to be dependent on whether the exposure time is equal to or less than the frame-to-frame time. As it is shown in Figure 11, the value of the f parameter significantly influences the correction distance. Thus a correction formula was constructed which fully accounts for short exposures relative to frame time and the other effects of rolling shutter. The amplitude of the correction distance ΔR_i is dependent on the row value of the bottom most row y_B, the rolling shutter row centroid y_i, the f parameter and the number of rows in the image:

$$\Delta R_i = \frac{\omega_{corr(i)}}{\omega_{ref}} \left(y_B - y_i - (1-f)\, n_{rows} \right) \tag{19}$$

The corrected coordinates of the meteor in Cartesian coordinates are then given by:

$$\begin{aligned} x_{corr} &= x_i + \Delta R_i \cos\varphi \\ y_{corr} &= y_i + \Delta R_i \sin\varphi \end{aligned} \tag{20}$$

It should be noted that the corrections defined herein are independent of where the user defines the origin of the focal plane Cartesian coordinate system. The origin can be the upper left corner, or the center, or some other location in the image. As long as centroid estimates and y_B are defined in the same coordinates.

A test of the performance of the spatial correction was done by applying it to simulated centroids of a decelerating meteor with an angle of $\varphi = 45°$. Computing the residuals in pixels between the true and the

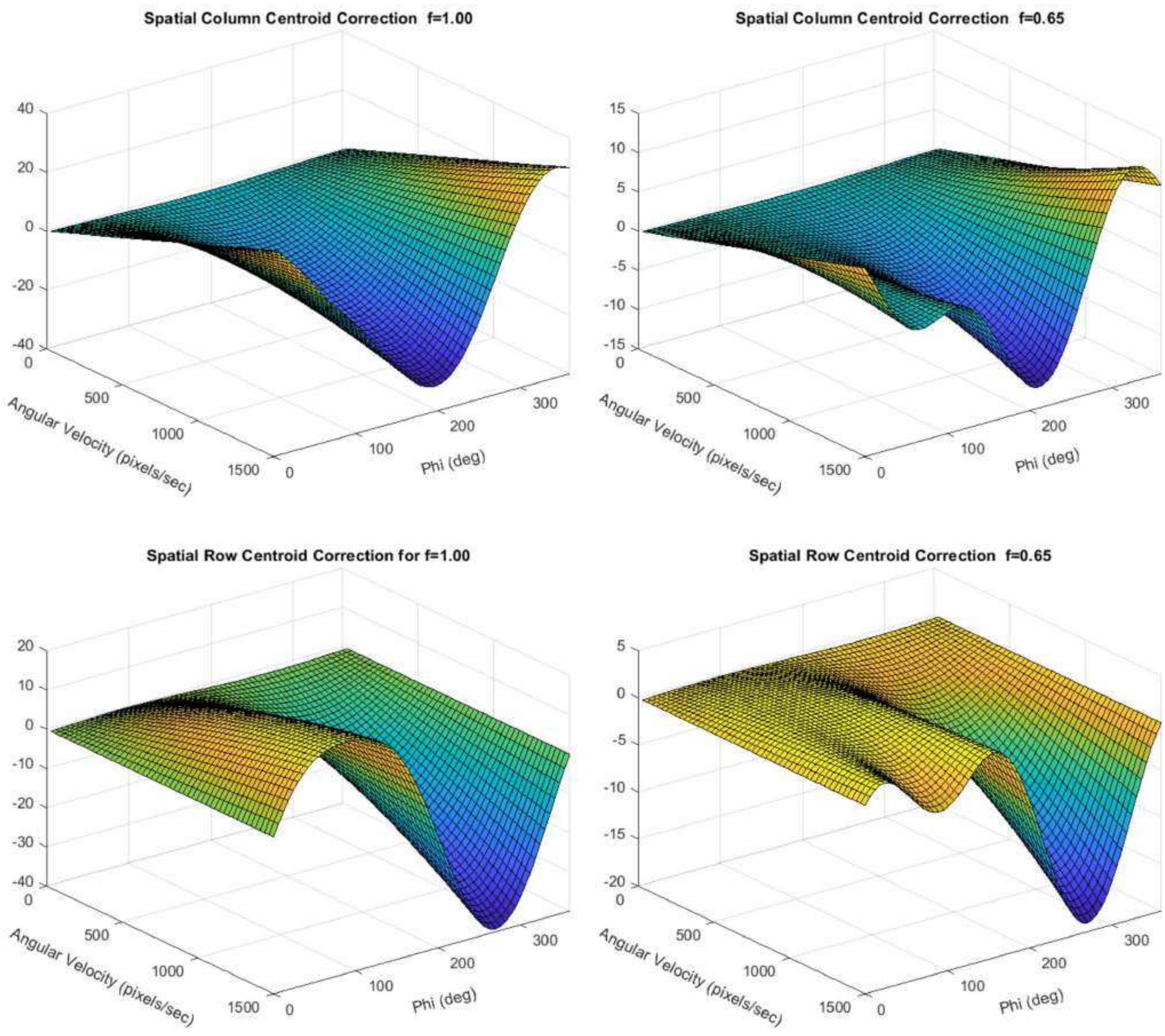

Figure 11 – Different correction distances depending on different values of the f parameter. Shown in relation to angular velocity and meteor angle.

corrected positions, the results are shown in Figure 12. The maximum centroid residual for the highest angular velocity is 0.3 pixels for the largest background noise level, slightly higher than the theoretically achievable precision. The reason for the deviation is the simplicity of the angular velocity smoothing method in a highly decelerating situation – the averaging of neighbouring angular velocities underestimates the true angular velocity due to non-symmetry in velocity before and after the time of interest.

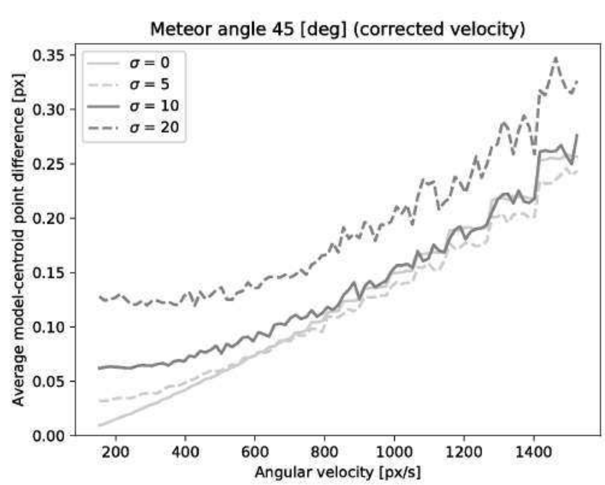

Figure 12 – The centroid offset in relation to the velocity. The spatial correction is applied to centroid coordinates.

2.4 When to apply the rolling shutter corrections

In this section we analyze when does the rolling shutter start to have a significant impact on velocity estimation for a meteor. For this analysis we will assume a worst case scenario of a meteor moving in a vertical direction of the focal plane ($\varphi = 90°$ or $270°$) with the fastest entry velocity of 72 km/s, 90° from the radiant and passing overhead with a range of 70 km.

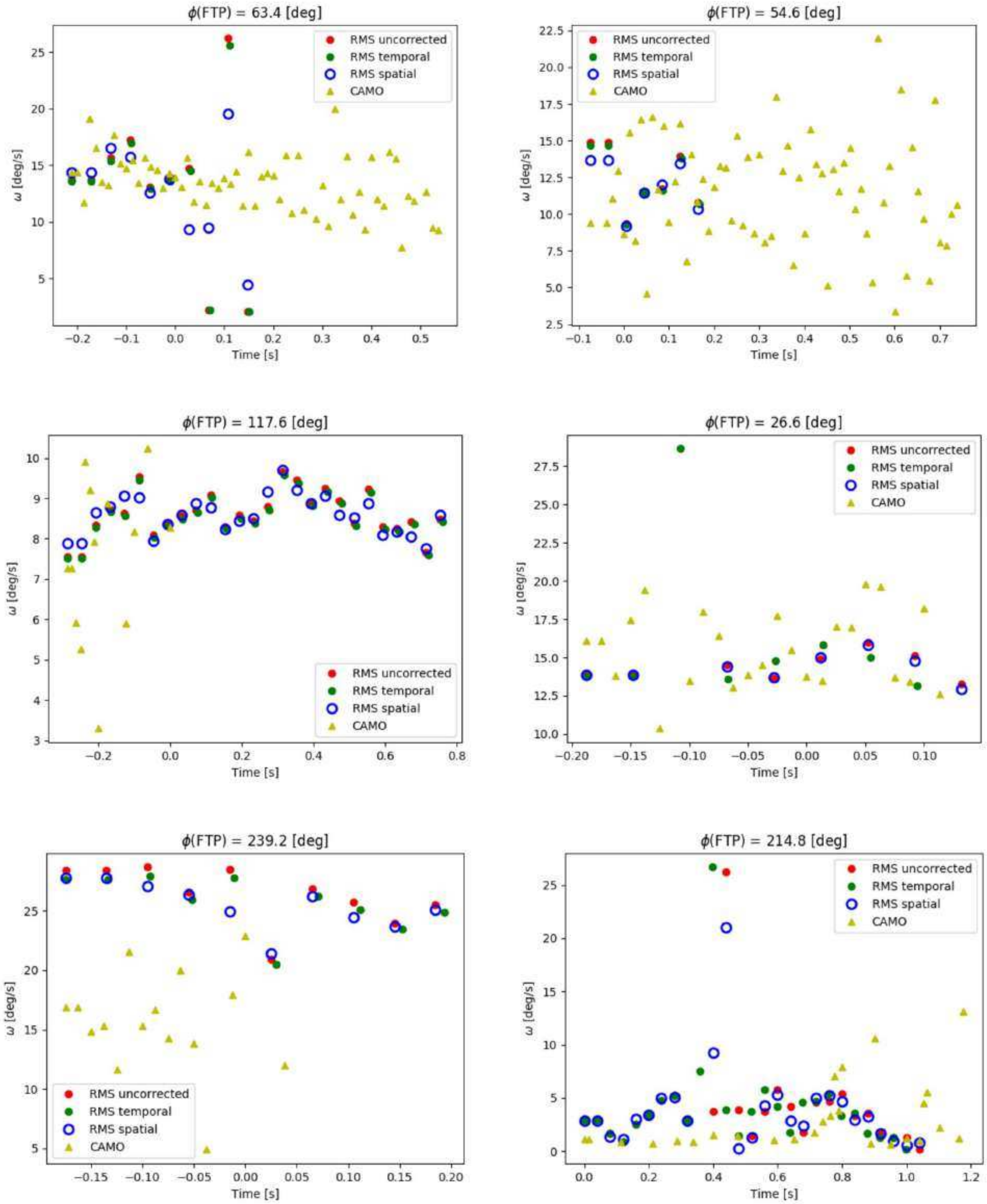

Figure 13 – Comparison of angular velocities obtained from corrected and uncorrected coordinates. 300 '/s corresponds to about 100 px/s. At this speed, the maximum offset in the angular velocity is only 0.2 px/s.

This meteor has the apparent angular velocity ω_{max} of $\sim 60^\circ/\mathrm{s} = 3600'/\mathrm{s}$.

Rearranging the terms in equation (16), and substituting the values mentioned above, we obtain the following expression for a threshold T:

$$T = \frac{\omega_{ref}}{\omega_{max}} = \frac{n_{rows} \times FPS \times k}{3600'/\mathrm{s}} < \frac{100\% - \omega_{err}}{\omega_{err}} \quad (21)$$

where ω_{err} is a given relative velocity error in percent, defined as:

$$\omega_{err} = 100\% \times \frac{\Delta\omega_{max}}{\omega_{max}} \quad (22)$$

When T is less than the right hand side, then the rolling shutter corrections should be employed. For given velocity error tolerances of $\omega_{err} = 5\%$, 2% and 1%, the right hand side limit is 19, 49 and 99, respectively. Table 1 shows the threshold T computed for various meteor camera systems as if they had rolling shutter sensors.

In general, all-sky systems with rolling shutter cameras do not need to apply corrections except in rare extreme cases with a very tight velocity tolerance of 1%. Moderate and narrow FOV systems do need to apply the corrections. The trend in cameras is to go to larger resolutions and higher frame rates. This helps push the threshold higher, but each designed system should be assessed using the equation above. Also, Sony has announced[a] that low cost global shutter cameras will be out soon, so the need for rolling shutter correction may all be moot in the future. For now, however, this should provide rough guidance as to when to apply the corrections.

3 Results

To verify that the corrected positions and timings of centroids are correct, the correction formulae have been applied to the measurements from an actual rolling shutter camera and compared to a global shutter camera's measurements. A Sony IMX225 rolling shutter camera with a 4 mm lens ($64^\circ \times 35^\circ$ FOV) was installed next to the Canadian Automated Meteor Observatory (CAMO) in Elginfield, Ontario, Canada (Weryk et al., 2013). The CAMO widefield camera is a global shutter camera operated at 80 FPS, with the IMX225 pointed to the same field of view as the CAMO widefield camera. Data from the IMX225 was collected and processed using the RMS meteor detection software (Vida et al., 2016).

To provide evidence of a properly formulated correction, several common meteors between CAMO and the IMX225 had their angular velocities computed. Both the temporal and spatial corrections were applied to measured meteor centroids in the respective image coordinate system for each common meteor. The image coordinates were then transformed to celestial equatorial coordinates using astrometric calibration fits using the RMS library[b].

The spatial and temporal corrections worked as expected by correcting RMS-derived angular velocities closer to CAMO angular velocities. After applying either correction the difference between the corrected and uncorrected angular velocities was rather negligible because moderate field of view cameras observe meteors with relatively low on-chip angular velocities, as was the case with the cameras used. The results are shown in Figure 13.

Utilizing double-station data from two RMS systems running rolling shutter cameras, one at Elginfield and the other at Tavistock (both in Ontario, Canada). The systems were 45 km apart and were observing the same volume of the sky, thus the meteor trajectories could be estimated. Having manually paired the events, the trajectories were computed using the least mean squares (Borovička, 1990) meteor trajectory estimation method. Five common events from the night of 2018 June 14 have been observed and their trajectories estimated. Figure 14 shows four of the meteors that were captured.

For every event, the initial velocity was estimated by fitting a line to the first 25% of time versus distance data. Next, the lag was computed (i.e. the difference between the observed time versus distance and the linear extrapolation using a constant initial velocity). As the rolling shutter effect should have an influence on the observed velocity and therefore the deceleration, we compared the observed lags from both sites. Figures 15 through 19 show the comparison of computed lags (i.e. deceleration profiles): left insets show uncorrected lags, middle insets show lags after the spatial correction, and right insets show lags after the temporal correction. As it can be seen, the lags do not show major differences, indicating that the meteor deceleration is not significantly influenced by the rolling shutter effect from the perspective of a particular observer for the camera specifications utilized.

The estimated geocentric radiants and velocities of the observed meteors are given in Table 2. Due to the small distance between the stations, all meteors have unfavourable geometry with convergence angles of only 10° to 15°, which increased the uncertainty in the estimated radiants. Nevertheless, we notice a significant difference in the geocentric velocity (up to 1 km/s), while radiant estimates seem to be rather stable.

4 Conclusion

Currently, the CCD sensors that have been widely used in meteor cameras, are beginning to be phased out, and meteor astronomers are considering the use of low-cost CMOS alternatives, which typically employ rolling shutters. Simulating the rolling shutter effect of CMOS cameras, it can be shown to have a large influence on meteor position measurements when the meteor has high on-chip apparent angular velocity. This paper provides both a spatial and a temporal method of meteor centroid correction. Both of the correction types account for exposure times that may be less than frame-to-frame times, and have been found to be robust to noise and deceleration.

The temporal correction is the simplest, which corrects only the time of the measurement centroid. It requires knowing only the row coordinate of the centroid and the number of rows in the image. However, using this correction approach will result in meteor centroid measurements being sampled non-uniformly in time. Note that astrometric conversion from focal plane coordinates to equatorial or alt-azimuth coordinates should use the rolling shutter estimated centroids. Only the time of the measurement is corrected.

Alternatively, the spatial correction can be used to correct the position of the rolling shutter centroid on the image, which maintains the uniform time sampling at the frame rate. This requires an estimate of the meteor angle and speed across the focal plane, the row

[a]Sony announcement: `https://www.sony.net/SonyInfo/News/Press/201802/18-018E/index.html`, accessed July 25, 2018

[b]RMS GitHub library: `https://github.com/CroatianMeteorNetwork/RMS`

Table 1 – Comparison of precision thresholds for different camera systems. FOV is the field of view of the vertical image direction.

System	FOV	n_{rows}	FPS	k ['/px]	T
All-sky Full HD	all-sky 180°	1080	25	10	75
RMS 720p, 1*	moderate 35°	720	25	2.9	15
CAMS 720p, 2*	moderate 22°	720	25	1.8	9
CAMS Full HD, 2*	moderate 22°	1080	25	1.2	9
Kowa 55mm f/1.0 720p, 3*	telescopic 4°	720	25	0.5	2.5
50mm ASI120	telescopic 2.5°	960	30	0.16	1.3

1* - (Vida et al., 2018); 2* - (Jenniskens et al., 2011); 3* - (Šegon et al., 2015)

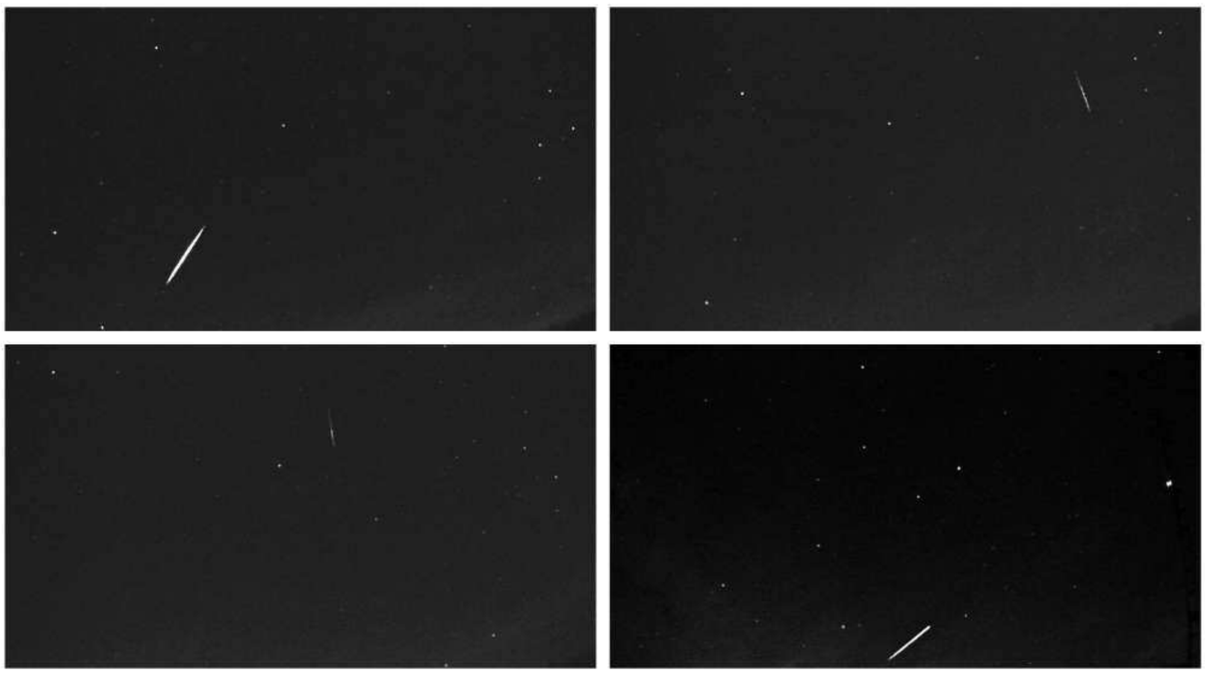

Figure 14 – Four of the meteors imaged with the two RMS systems on 2018 June 14.

of the rolling shutter centroid, the row coordinate of the bottom row in the image, the number of rows in the image, frame rate, exposure to frame time ratio, and pixel angular extent. The "corrected" positions of the rolling shutter centroids are used to generate equatorial or alt-azimuth coordinates via standard astrometry.

To confirm the validity of these corrections we have first tested them on simulated video sequences of meteors in various speeds, orientations, and sensor configurations. Then we compared angular velocities of real observed meteors obtained using a rolling shutter camera and a global shutter camera. We also applied the spatial and temporal corrections on real double station meteor observations collected using rolling shutter cameras. Using the formulations provided herein, correct track positions and apparent angular velocities were obtained. It is apparent that the rolling shutter effect can impact the estimated velocity and should be corrected for using the provided methods.

5 Acknowledgements

We thank Dr. Peter Brown and Dr. Margaret Campbell-Brown for kindly allowing us to use CAMO data.

6 Author Contributions

PK did most of the coding and wrote most of the manuscript, PG developed the temporal correction, improved the spatial correction, added the correction for short exposure times, independently confirmed the Python simulations and performed final edits on the paper, DV provided the initial code, provided guidance and wrote parts of the manuscript, DŠ provided guidance and coordination, and AM tested IP cameras and other hardware used for this work.

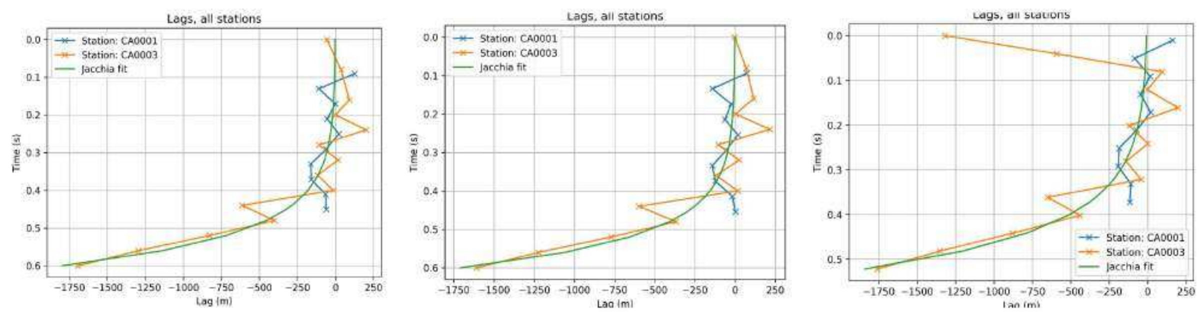

Figure 15 – Meteor of 2018 June 14, $06^h07^m20^s$ UTC; Left: Uncorrected meteor coordinates. Middle: Spatially corrected coordinates. Right: Temporally corrected coordinates.

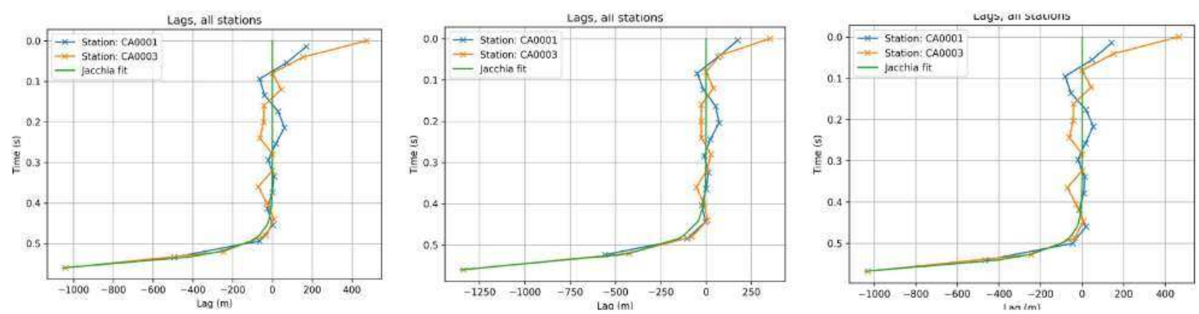

Figure 16 – Meteor of 2018 June 14, $06^h26^m58^s$ UTC; Left: Uncorrected meteor coordinates. Middle: Spatially corrected coordinates. Right: Temporally corrected coordinates.

References

Borovička J. (1990). "The comparison of two methods of determining meteor trajectories from photographs". *Bulletin of the Astronomical Institutes of Czechoslovakia*, **41**, 391–396.

Brown P., Weryk R., Kohut S., Edwards W., and Krzeminski Z. (2010). "Development of an all-sky video meteor network in Southern Ontario, Canada The ASGARD System". *WGN, Journal of the International Meteor Organization*, **38**, 25–30.

Ceplecha Z. (1987). "Geometric, dynamic, orbital and photometric data on meteoroids from photographic fireball networks". *Bulletin of the Astronomical Institutes of Czechoslovakia*, **38**, 222–234.

Jacchia L. G. and Whipple F. L. (1961). "Precision orbits of 413 photographic meteors". *Smithsonian Contributions to Astrophysics*, **4**, 97–129.

Jenniskens P., Gural P., Dynneson L., Grigsby B., Newman K., Borden M., Koop M., and Holman D. (2011). "CAMS: Cameras for Allsky Meteor Surveillance to establish minor meteor showers". *Icarus*, **216:1**, 40–61.

Samuels D., Wray J., Gural P. S., and Jenniskens P. (2014). "Performance of new low-cost 1/3" security cameras for meteor surveillance". In *Proceedings of the 2014 International Meteor Conference, Giron, France*. pages 18–21.

Šegon D., Andreić Ž., Korlević K., and Vida D. (2015). "Croatian Meteor Network: ongoing work 2014–2015". In *Proceedings of the International Meteor Conference, Mistelbach, Austria*. pages 27–30.

Vida D., Mazur M., Segon D., Zubovic D., Kukic P., Parag F., and Macan A. (2018). "First results of a Raspberry Pi based meteor camera system". *WGN, Journal of the International Meteor Organization*, **46:2**, 71–78.

Vida D., Zubović D., Šegon D., Gural P., and Cupec R. (2016). "Open-source meteor detection software for low-cost single-board computers". In *Proceedings of the International Meteor Conference (IMC2016), Egmond, The Netherlands*. pages 2–5.

Weryk R., Campbell-Brown M., Wiegert P., Brown P., Krzeminski Z., and Musci R. (2013). "The Canadian automated meteor observatory (CAMO): system overview". *Icarus*, **225:1**, 614–622.

Handling Editor: Javor Kac
This paper has been typeset from a LaTeX file prepared by the authors.

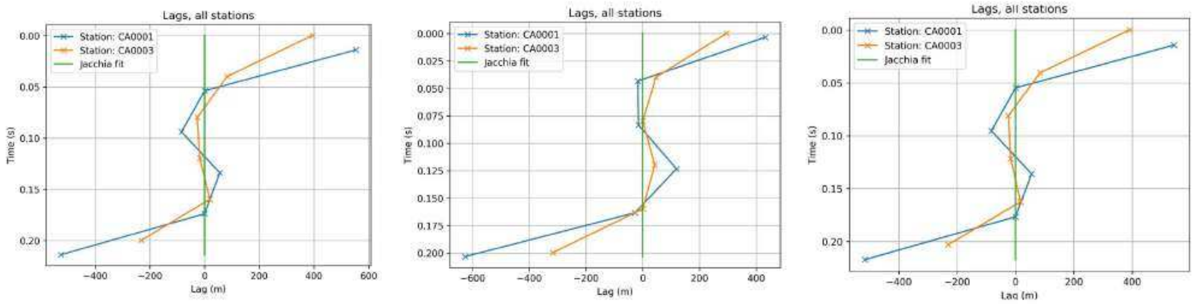

Figure 17 – Meteor of 2018 June 14, $07^h28^m09^s$ UTC; Left: Uncorrected meteor coordinates. Middle: Spatially corrected coordinates. Right: Temporally corrected coordinates.

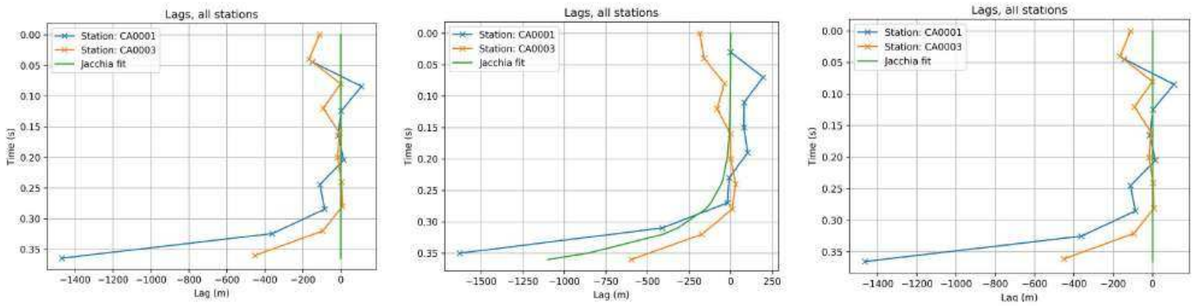

Figure 18 – Meteor of 2018 June 14, $07^h46^m21^s$ UTC; Left: Uncorrected meteor coordinates. Middle: Spatially corrected coordinates. Right: Temporally corrected coordinates.

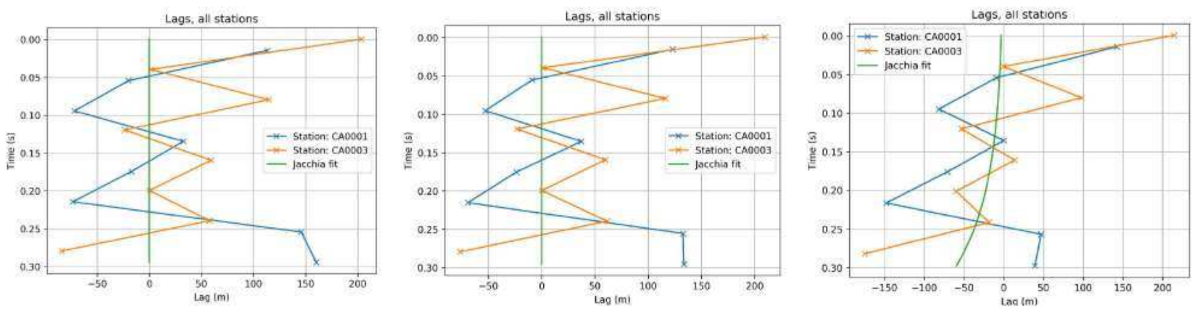

Figure 19 – Meteor of 2018 June 14, $07^h52^m12^s$ UTC; Left: Uncorrected meteor coordinates. Middle: Spatially corrected coordinates. Right: Temporally corrected coordinates.

Table 2 – Comparison of geocentric radiants and velocities for observed meteors. RA and Dec are given in degrees and V_g in km/s. The "Corr" column indicates the type of correction applied: O – original (no correction), S – spatial, T – temporal.

Time	Corr	RA_g	Dec_g	V_g
	O	228.14	+0.66	11.42
2018-06-14 $06^h07^m20^s$	S	228.53	+0.65	11.85
	T	227.61	+2.72	11.75
	O	315.36	+35.90	54.39
2018-06-14 $06^h26^m58^s$	S	315.38	+35.50	53.61
	T	315.37	+35.90	53.56
	O	317.77	+31.49	53.77
2018-06-14 $07^h28^m09^s$	S	317.85	+31.19	52.92
	T	317.77	+31.48	52.80
	O	11.91	+76.83	28.60
2018-06-14 $07^h46^m21^s$	S	13.03	+77.05	28.81
	T	11.91	+76.72	28.36
	O	274.54	−11.34	32.52
2018-06-14 $07^h52^m13^s$	S	274.52	−11.09	32.42
	T	274.31	−10.66	32.57